Colloidal Stability of PFSA-Ionomer Dispersions

Part II: Determination of Suspension pH Using Single-Ion Potential Energies

Harsh Srivastav[1,2], Adam Z. Weber[2], and Clayton J. Radke*[,1]

[1]Department of Chemical and Biomolecular Engineering,
University of California, Berkeley, 201 Gilman, South Dr., CA 94720

[2]Energy Technologies Area,

Lawrence Berkeley National Laboratory, Building 30, Cyclotron Road, Berkeley, CA 94720

Abstract

Perfluorosulfonic acid (PFSA) ionomers serve a vital role in the performance and stability of fuel-cell catalyst layers. These properties, in turn, depend on colloidal processing of precursor inks. To understand the colloidal structure of fuel-cell catalyst layers, we explore the aggregation of PFSA ionomers dissolved in water/alcohol solutions and relate the predicted aggregation to experimental measurements of solution pH. Not all side chains contribute to measured pH because of burying inside particle aggregates. To account for the measured degree of dissociation, a new description is developed for how PFSA aggregates interact with each other. The developed single-counterion electrostatic repulsive pair potential from Part I is incorporated into Smoluchowski collision-based kinetics of interacting aggregates with buried side chains. We demonstrate that the surrounding solvent mixture affects the degree of aggregation as well as the pH of the system primarily through the solution dielectric permittivity that drives the strength of the interparticle repulsive energies. Successful pH prediction of Nafion™ ionomer dispersions in water/n-propanol solutions validates the numerical calculations. Nafion™-dispersion pH measurements serve as a surrogate for Nafion™ particle-size distributions. The model and framework can be leveraged to explore different ink formulations.

*Corresponding author: Clayton Radke, radke@berkeley.edu

1. Introduction

Proton-Exchange-Membrane Fuel Cells (PEMFC) offer an attractive alternative to traditional internal-combustion engines in power generation as they often have higher efficiencies and fewer emissions that are less harmful or can more easily be contained.[1] PEMFCs harness the electrochemical reaction of oxygen and hydrogen to produce water, a byproduct harmless to the environment.[1] The catalyst layer (CL) in a PEMFC is critical to overall cell performance.[2]

CLs are most often composed of carbon-supported platinum (Pt) catalyst particles interspersed in a perfluorosulfonic-acid-polymer (PFSA) binder (ionomer) matrix. The chemical identity of the ionomer greatly affects the structure, stability, and performance of the PEMFC and, thus, is a topic of great interest in the community.[1–10] PFSAs, most notably Nafion™, which is most commonly used in the field, have remarkable electrochemical stability, and have been extensively studied since their employment in the late 1960s.[11] CLs are fabricated by suspending Pt-supported carbon particles in a mixed water/alcohol dispersion containing PFSA polymer followed by drying. Although there are decades of research on PEMFC catalyst layers, the complicated formation process remains poorly understood and relies entirely on empirical optimization, thereby limiting the introduction of new materials and structures that could minimize Pt loadings.

Because of their essential role in producing PEMFC catalyst layers, we focus here on dispersions of PFSA suspended in water/alcohol mixtures. Figure 1 illustrates the molecular structure of Nafion™ polymer. Although the appended side chain is somewhat hydrophilic, the fluorinated hydrophobic backbone means that the molecular solubility of Nafion™ PFSA in water/alcohol solutions is limited. The result is aggregation into suspended particles.[12–22] PFSA

sulfonate side chains are strong acids with pK_As near -6 in water.[18] Thus, a key feature of PFSA polymers is their ability to dissociate protons into the dispersion solution without an anion present.[23] Although solution-dissociated protons cannot stray far from the ionized sulfonate groups, the neutralizing acidic corona surrounding the particles still allows for readings on a pH probe.[23] Figure 2, described in more detail later, reports pH measurements of Nafion™ dispersed in four water/n-propanol mixtures as a function of polymer concentration.[18] Because of the strong acid side groups, increasing Nafion™ concentration lowers the solution pH significantly. More water-rich suspensions are more acidic. Since the dissociated protons are electrically balanced by the charges on the PFSA side chains, understanding the pH trends and the hydronium-ion charge distributions surrounding the ionomers is crucial to uncovering ionomer interactions. Solution pH influences how PFSA particles interact with each other,[24] which in turn controls Nafion™ particle sizes.

$$[(CF_2 - CF)_d - (CF_2 - CF)]_m$$
$$| $$
$$O - CF_2 - CF - CF_3 \qquad H^+$$
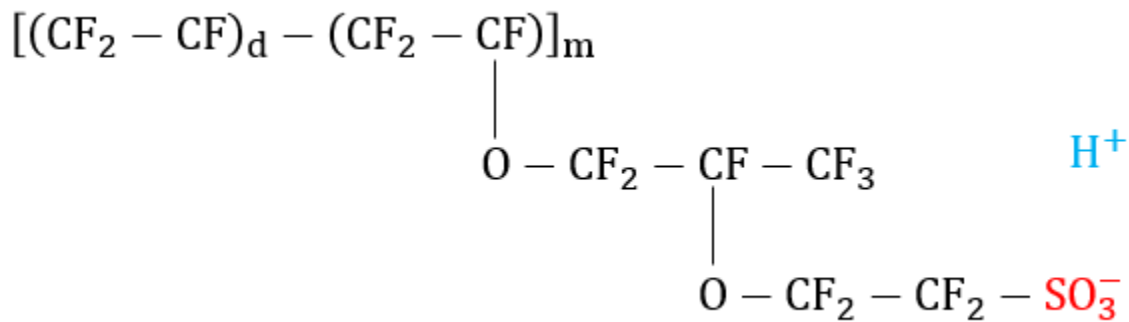$$| $$
$$O - CF_2 - CF_2 - SO_3^-$$

Figure 1: Molecular structure of Nafion™. The fluorinated backbone is hydrophobic, allowing for the formation of tightly bound aggregates. The appended side chain is hydrophilic, with a number fraction given by the equivalent weight, terminating in sulfonate groups.

Because of the very negative pK_A of the sulfonic-acid groups, essentially all protons dissociate from the appended side chains when they are exposed to an aqueous solution. The

ratio of side-chain groups to polymer backbone is known from measured equivalent weights (EW, defined as the grams of PFSA polymer per mole of sulfonic-acid groups[25]). However, a
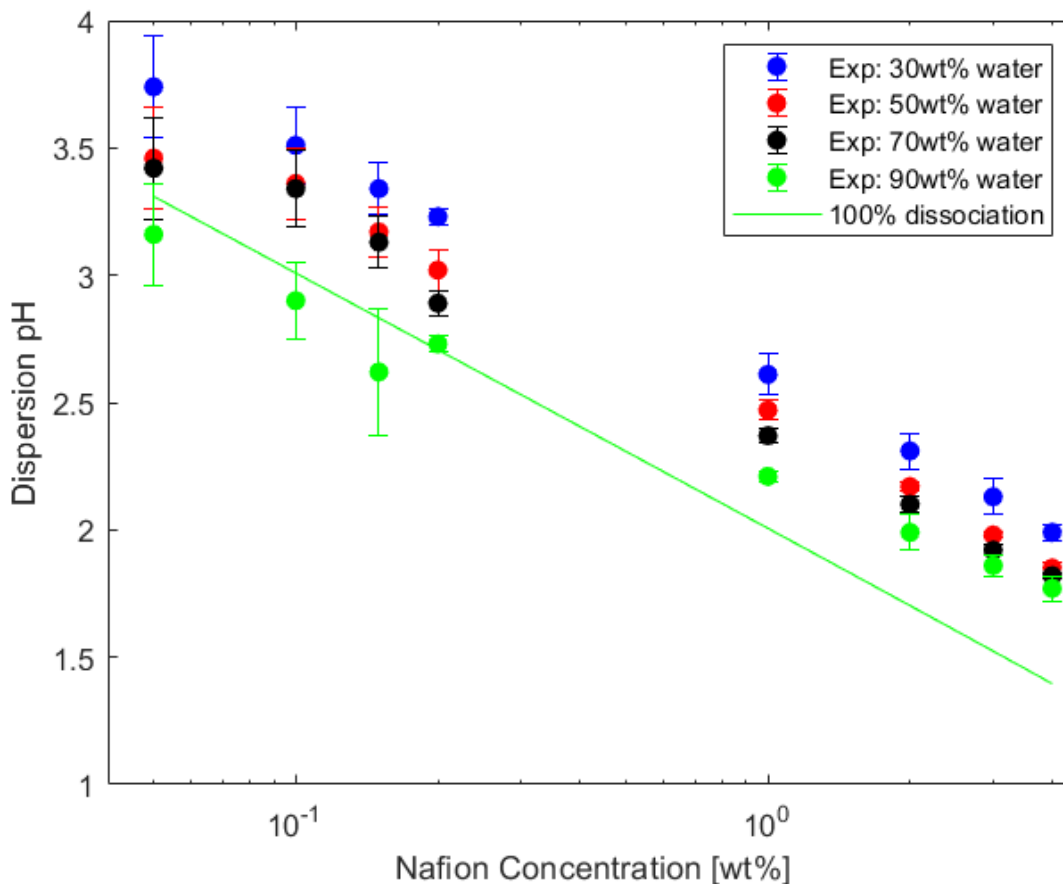

Figure 2: Dispersion experimental pH (filled circles) as a function of Nafion™ concentration in four water/n-propanol solutions after Berlinger et al. with permission.[23] The solid line for 90 wt% water corresponds to 100% dissociation of sulfonate side groups; 100% dissociation lines for the other solutions deviate only slightly.

simple calculation, shown by the solid line in Figure 2, reveals that complete side-group ionization overpredicts the measured solution acidity.[18] The propensity to dissociate from side chains should remain the same regardless of polymer concentration or dispersion medium. Thus, based on the work of Berlinger et al.,[23] we propose a mechanism in which a fraction of the dissociated protons

bury inside the PFSA aggregates and cannot be detected by a pH probe. Figure 3 illustrates the idea. We hypothesize that only hydronium ions exposed at the external surface area of Nafion™ particles are detectable by a pH probe. Conversely, hydronium ions buried inside enclosed-chain regions cannot escape and, therefore, are not detectable. Some aggregate configurations, even that of single Nafion™ chains, exhibit enclosed domains and localize hydronium counterions.[23] For larger Nafion™ aggregates, more protons trap inside. Larger aggregate sizes imply smaller surface-area-to-volume ratios, yielding lower external concentrations of dissociated mobile protons, as depicted in Figure 3. This means that the fractional dissociation of an aggregate is always less than or equal to β_1, the fraction dissociated for a single Nafion™ chain. Essentially, Nafion™ aggregates serve as the precursors for later processing into single-ion conducting ionomers (and membranes).[26–28] Another strong influence in Figure 2 for the suspension mobile-charge-fraction dissociation is the solution dielectric permittivity. High dielectric-constant dispersions, such as those with high water content, apparently produce smaller aggregate sizes that allow for larger side-chain solution exposure and, therefore, lower pH values.
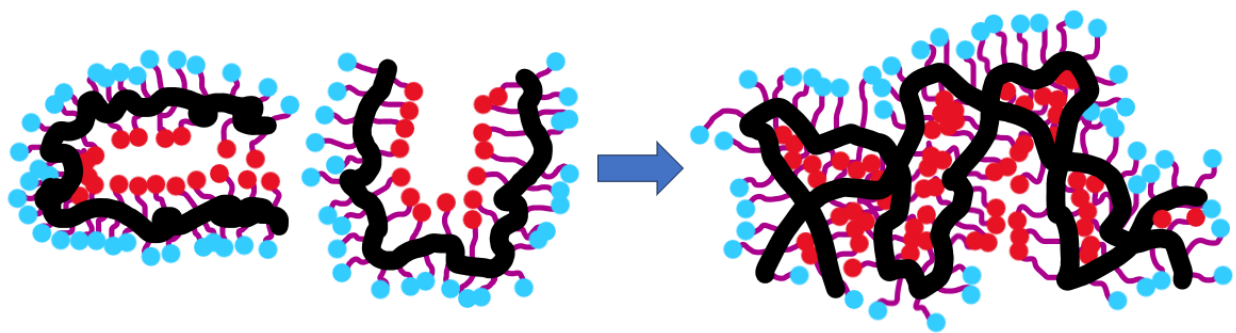

Figure 3: Nafion™ aggregation schematic showing polymer chains with backbone (black) and side groups (purple). Sulfonate groups with free dissociating protons (not shown) that contribute to measured pH are colored blue, whereas sulfonate groups with dissociated but buried protons that do not contribute are colored red. Non-pH contributing side groups (buried) occur both in single chains and more so in aggregated particles.

The pH of PFSA dispersions is thus helpful both to expose surface-charge densities of Nafion™ aggregates, as well as to unveil aggregate-size distributions. Other size- and charge-characterization techniques, including Dynamic Light Scattering (DLS) and electrophoresis, are difficult to reproduce and thus show significant disagreement.[14–23,29,30] For more concentrated suspensions, SAXS and USAXS data, and other X-ray techniques (e.g., ptychography, STXM, etc.), fail to provide definitive fits to model-size parameter predictions.[16,31,32] Other techniques, such as electron microscopy impose too much beam damage to be reliable.[33] Neutron scattering is likewise infected by different interpretations.[34] As a result, we use pH as an indirect characterization of PFSA particle size and surface-charge density,[23] with the hope that future experimental methods will allow for confirmation and comparison of the modeling results presented in this work.

2. Dispersion Preparation

The process of constructing CLs and even the precursor dispersions can vary significantly among different researchers.[35] We focus on the preparation process utilized by Berlinger *et al*.[23] Nafion™ -D2021 (EW = 1,000 g/eq) dispersion stock solutions (Ion Power Inc., New Castle, DE) were diluted to the desired concentration by water/n-propanol solutions of choice and sonicated for 1 h to breakup pre-formed aggregates. This process allows for uniformity in initial conditions given that stock solutions may change over long time periods and, thus, are aggregated to different extents. Once prepared, no visual suspension particle settling is observed. Approximately 30 s after sonication, pH measurements are gathered under continuous gentle stirring. Measurements taken on the order of minutes/hours show little change in pH. Details of pH calibration in the various

solvent mixtures and suspension pH measurements have been described.[35] Here we use "particle" or "aggregate" to mean both a group of Nafion™ chains or a single Nafion™ chain (which is then a particle aggregate of one chain).

3. Theory

Figure 3 illustrates that PFSA aggregates must grow to predict suspension pH: larger aggregates internally confine relatively more protons in their increasing interstitial voids. Figure 3 also illustrates that PFSA agglomerates are not spherical, but cylindrical-like with branching side chains.[14–23,29,30] Nevertheless, because the aspect ratio of the rod-like agglomerates is not large, approximately 1.3,[14] we treat the growing particles as effective spheres with one, but important, exception outlined below in Section 3.2. In our evaluation of suspension pH, hydrogen ions trapped in the agglomerate interstitial voids do not contribute to probe-measured pH.

3.1 Aggregation Kinetics

As particles aggregate and grow from single chains, some fraction of the aggregate charge buries and some fraction remains externally exposed, as sketched in Figure 3. Only hydrogen ions dissociated from the external-surface-exposed sulfonate groups contribute to measured pH. Buried hydrogen ions inside the aggregated particles do not contribute to the solution pH. As aggregation continues, relatively more Nafion™ side-group charges bury.

Smoluchowski irreversible batch kinetics is adopted to model particle growth in time until particle growth ceases. In Smoluchowski kinetics, particle growth occurs by binary collisions with rate constants that depend exponentially on pair interaction energies between the different size aggregates:[36–39]

$$\frac{dC_k}{dt} = \sum_{i=1,j=k-i}^{k-1} \frac{K_{ij}}{W_{ij}} C_i C_j - \sum_{i=1}^{\infty} \frac{K_{ik}}{W_{ik}} C_i C_k \qquad (1)$$

where

$$K_{ij} = \frac{2k_B T}{3\mu} \frac{(a_i + a_j)^2}{a_i a_j} \qquad (2)$$

and

$$W_{ij} = (a_i + a_j) \int_{a_i+a_j}^{\infty} \frac{\exp\left(\frac{U_{tot}(r)}{k_B T}\right)}{r^2} dr \qquad (3)$$

C_k denotes the number concentration of aggregate-size k per suspension volume, K_{ij} is the diffusion-based collision rate constant between particles i and j, W_{ij} is the stability factor between particles i and j, a_i is the equivalent radius for aggregate i of a sphere of the same volume, μ is the viscosity of the solvent, k_B is Boltzmann's constant, T is absolute temperature, and $U_{tot}(r)$ is the interparticle pair interaction potential energy, where r is the interparticle center-to-center radius. Equations 1-3 apply to perikinetic coagulation in quiescent dispersions,[36,37] whereas pH measurements were conducted with continuous stirring. Nevertheless, perikinetic aggregation is applicable for small particles, even with some stirring.[37] Perikinetics also provides a conservative time estimate of the aggregation process.

The important factor in Equations 1-3 is the interparticle pair-interaction potential energy. Clearly, large potential-energy barriers in $U_{tot}(r)$ produce large stability factors that greatly slow particle kinetics. Classically, $U_{tot}(r)$ consists of an attractive van der Waals or Hamaker contribution, $U_{vdw}(r)$ and a repulsive electrostatic potential energy when the particles are of the same charge sign, $U_r(r)$,[36]

$$U_{tot}(r) = U_{vdw}(r) + U_r(r) \qquad (4)$$

One expression for the attractive interaction potential is

$$U_{vdw}(r) = -\frac{A_H}{6}\frac{a_i a_j}{(a_i + a_j)}\frac{1}{(r - a_i - a_j)} \tag{5}$$

with the Hamaker constant A_H written as[40]

$$A_H = \frac{3}{4}k_B T \frac{\left(\epsilon_p - \epsilon_m\right)^2}{\left(\epsilon_p + \epsilon_m\right)^2} + \frac{3\pi\hbar\nu_e}{8\sqrt{2}}\frac{\left(n_p^2 - n_m^2\right)^2}{\left(n_p^2 - n_m^2\right)^{\frac{3}{2}}} \tag{6}$$

where ϵ_m is the dielectric permittivity of the medium, ϵ_p is the dielectric permittivity of the particle, $\hbar$ is the reduced Planck's constant, n_p is the refractive index of the particle, and n_m is the refractive index of the medium. The constant used for the absorption frequency is denoted by ν_e, here taken to be $5 \times 10^{15} s^{-1}$.[38] For water and n-propanol, we have $\epsilon_m = 78.4\epsilon_o, \epsilon_p = 20.2\epsilon_o$, respectively, and $n_m = 1.333, n_m = 1.387$, respectively, where ϵ_o is the dielectric permittivity of free space.[41–43] All properties of water/n-propanol mixtures are volume averages of the pure species. Since these parameters are not well known for Nafion™, we use the same parameters that give the Hamaker constants in Shukla, *et al.* for Carbon Black[38] with the assumption that the overall Hamaker constant, since it only depicts long-range intermolecular forces, does not vary greatly among substances. Unfortunately, classical DLVO theory[36–38] fails to quantify the electrostatic interactions between Nafion™ aggregates because no background electrolyte is present and because the system is closed. Thus, construction of an applicable expression for $U_r(r)$ is paramount.[24]

Each PFSA aggregate is surrounded by a diffuse double layer of solution hydronium ions that dissociated from the surface to self-neutralize each aggregate. No other electrolyte is present in the solution, so the double-layer corona consists only of a single counterion. With only a single-counterion species present, the double layer cannot extend out to an electrically neutral solution region. Rather, the hydrogen-ion cloud first encounters double layers extending from nearby particles. Consequently, the classical DLVO framework cannot be used for Nafion™ suspensions.

In Part I of this contribution, we calculate $U_r(r)$ for two single-ion-electrolyte interacting spherical particles using Poisson-Boltzmann theory:[24]

$$U_r\left(r = h + a_i + a_j\right) = \frac{2\pi a_i a_j}{a_i + a_j} k_B T \int_h^{2L} (y - h)(c_m(y) - c_L)\, dy \tag{7}$$

where c_L is the number concentration of hydronium ions per unit solvent volume at the overlap distance L and $c_m(y)$ is the midplane hydronium-ion number concentration per unit solvent volume between two flat plates of equal surface-charge density q immersed in a continuum polar liquid and separated by distance y. Part I discusses in detail the calculation of $U_r(h)$ for various surface-charge densities, particle sizes, and suspension volume fractions.[24] We emphasize that the single-ion electrostatic potential energy $U_r(h)$ is quite different than the corresponding classical added-electrolyte potential energy. Among these differences are that electrostatic pair potentials in single-counterion theory exhibit a much stronger size dependence than do classical added-electrolyte potentials. More importantly, they depend strongly on particle volume fraction.[24] This means that all interparticle pair potential energies must be re-calculated during kinetic evolution of each new size distribution in Equation 1, as outlined below.

Example total potential energies, including the additive single-ion potentials and Hamaker forces, $U_{tot}(h)$, are illustrated in Figure 4. Note the surprising effect that increasing the suspension volume fraction decreases the electrostatic repulsion and hence the total interaction potential.
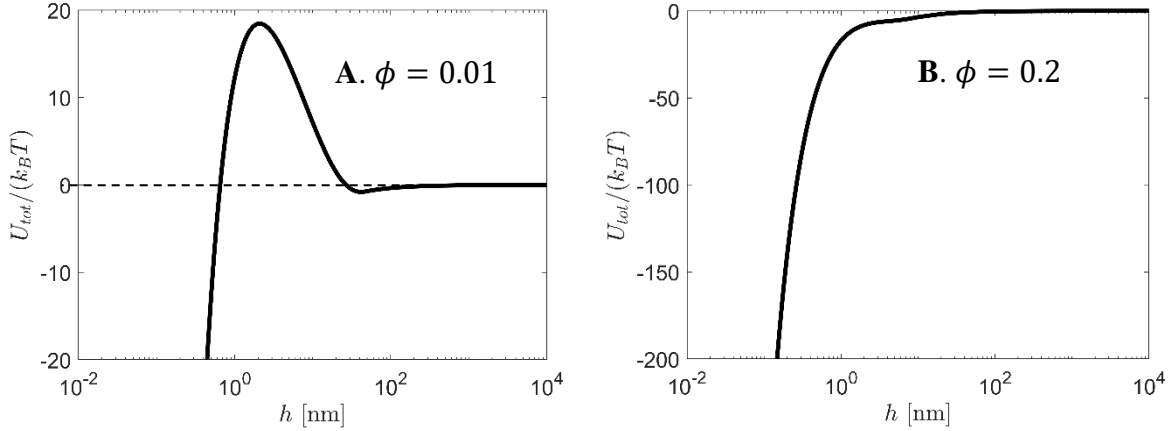
Figure 4: Normalized total interaction energies including Hamaker attractive forces between two equal-size Nafion™ spheres of diameter 10 nm at 50 wt% water in n-propanol with **A**. $\phi = 0.01$ **B**. $\phi = 0.2$.

Figure 4 applies specifically to equal size spheres. Here, we are interested in low-aspect-ratio cylindrical particles of unequal and changing size as aggregation proceeds. The key idea is that particles are surrounded on average by other interacting particles a volume-average distance, *L*, away.[24] From SANS/SAXS data, multiple authors[2,14,16] report a rod-like configuration for Nation aggregates. Accordingly, rather than estimate *L* for a collection of spheres, we estimate the overlap distance for collection of low-aspect-ratio cylinders.

3.2 Cylindrical Estimate of Overlap Distance

Yamaguchi *et al.* give a helpful correspondence between the amount of mass in a Nafion™ aggregate and the radius/length of the rod that it forms: an aggregate of 300,000 amu forms a rod with radius of 2.5 nm and a length of 6.5 nm (i.e., for an AC240 Nafion™ sample),[14] giving an aspect radius of 1.3. Since this radius and length are found through a heat-treatment of the system, which is thought to break up the Nafion™ aggregates into individual chains, we use them to characterize the size of the rod of a single chain. All aggregates then have an integer multiple of the number of equivalents of a single chain. For a fixed aspect ratio, the radii and lengths of other aggregates of *i* single chains are found from the expressions:

$$R_i = R_1 \sqrt[3]{i} \tag{8}$$

and

$$L_i = L_1 \sqrt[3]{i} \tag{9}$$

where R_i is the cylindrical radius of the rod, and L_i is the length of the rod. As illustrated in Figure 5, L is established for a given volume-fraction suspension, through partitioning the space around each aggregate according to the expression:

$$\phi = \frac{\sum_{i=1}^{N} C_i R_i^2 L_i}{\sum_{i=1}^{N} C_i (R_i+L)^2 (L_i+2L)} = \sum_{i=1}^{N} C_i R_i^2 L_i \tag{10}$$

where C_i is the number concentration of an Nafion™ aggregate consisting of i single chains. The denominator in the first right term equals unity because the size distribution is in suspension concentration units. This result reveals that L decreases as the concentration of Nafion™ increases. Suspension volume fraction is conserved during aggregation upon neglect of solvent trapped in aggregates. We calculate the suspension volume fraction from initially prepared single chains given the known suspension mass fraction and densities of pure water (1000 kg/m³) and dry Nafion™ (2100 kg/m³)[7] assuming ideal mixing.

$$\phi = \frac{\frac{w_{Nf}}{\rho_{Nf}}}{\frac{w_{Nf}}{\rho_{Nf}} + \frac{w_w}{\rho_w} + \frac{w_{prop}}{\rho_{prop}}} \tag{11}$$

where w_{Nf}, w_w, w_{prop} denote the weight fractions of Nafion, water, and n-propanol, respectively, while $\rho_{Nf}, \rho_w, \rho_{prop}$ denote the mass densities of Nafion, water, and n-propanol, respectively. Equations 8-11 permit calculation of the overlap distance for each aggregate size distribution.
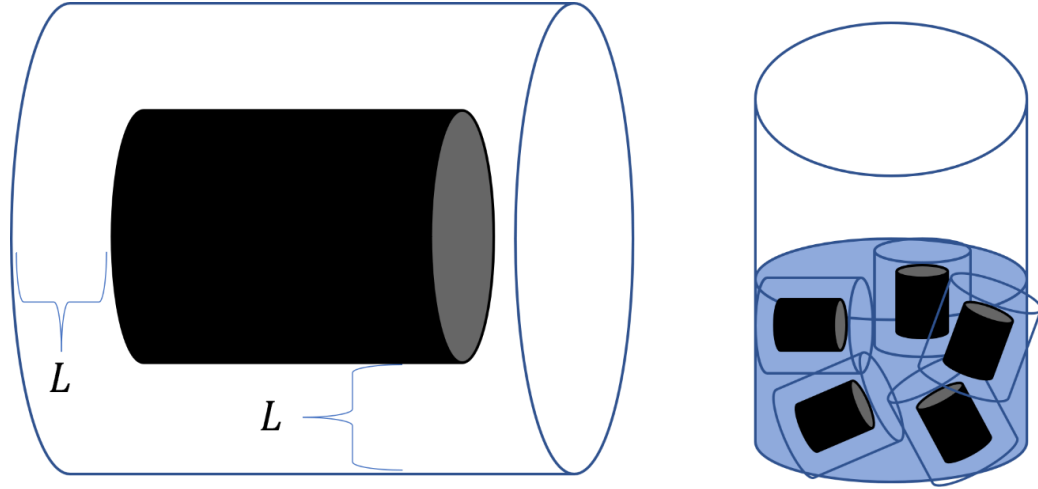
Figure 5: (Left) A Nafion™ aggregate surrounded by a cylinder with length and radius extended by L to denote the region where dissociated protons encounter nearby double layers. (Right) The partition of the volume in the solution by cylinders of the form on the left. Although perfect partitioning is not expected at any particular moment (as can be seen by the crossovers of the cylinders on the right), on average they are a distance L apart.

Likewise, we establish each cylindrical aggregate surface-charge density, q, from the relation:

$$q = -\beta_1 \frac{eN_{SO_3^-}}{2\pi R_1 (R_1 + L_1)} \tag{12}$$

where $N_{SO_3^-}$ is the total number of sulfonate groups in a single chain, dissociated or not, obtained from the Nafion™ equivalent weight and molecular weight (for a $1{,}000$ g/eq for Nafion™ D2021[44] of 300 kDa, $N_{SO_3^-} = 300$). As pictured in Figure 3, not all appended $-SO_3^-$ side groups are exposed to the external surface. β_1 reflects the fraction of charged sulfonate groups exposed for a single chain and is fit to match one measured pH in one solvent. Once β_1 is determined, q is known from Equation 12 and taken to be the same for all subsequent aggregate sizes, meaning that

relatively more $-SO_3^-$ groups are trapped as particle sizes grow and do not contribute to measured pH. From Equations 8, 9, and 11, the fraction of exposed charges for aggregate size i falls with increasing aggregate number as $\beta_i = \beta_1/\sqrt[3]{i}$. The simple calculation reflected by the straight line in Figure 2 corresponds to $\beta_i = 1$.

3.3 Evaluation of Pair Potentials $U_{tot}(r)$

Once L is determined reflecting a given size distribution, the average cylinder radius, R_c, follows from definition

$$R_C \equiv \frac{\sum_{i=1}^{N} C_i R_i}{\sum_{i=1}^{N} C_i} \tag{13}$$

This radius allows calculation of the hydrogen-ion molecular concentration, c_L, at the distance L from the Poisson-Boltzmann expression for parallel cylinders or

$$\frac{1}{r}\frac{d}{dr}\left(r\frac{d\Phi}{dr}\right) = -\frac{ec_L}{\epsilon}\exp\left(-\frac{e\Phi}{k_BT}\right) \tag{14}$$

with boundary conditions

$$\Phi(R_c + L) = \Phi'(R_c + L) = 0 \tag{15}$$

and

$$q = -\epsilon\frac{d\Phi}{dr}\bigg|_{r=R_C} \tag{16}$$

where again R_C is the average cylinder radius, Φ is the electrostatic potential relative to the distance L, and ϵ is the dielectric permittivity of the solvent. c_L is determined numerically from Equations 13-16 for later use in Equation 7, as detailed in the SI.

The exact geometry of PFSA aggregates is not settled.[16,34] In the case of other particle geometries, the equations above can be modified. For the example of spheres, Equations 8 and 9 are unnecessary, and we simply deal with a_i. Equation 10 can be rewritten as

$$\phi = \frac{\sum_{i=1}^{N} C_i a_i^3}{\sum_{i=1}^{N} C_i (a_i + L)^3} = \sum_{i=1}^{N} C_i a_i^3 \tag{17}$$

Equation 12 then becomes

$$q = -\beta_1 \frac{e N_{SO_3^-}}{4\pi a_1^2} \tag{18}$$

Also for spheres (adjusting the boundary conditions accordingly as well), we have

$$\frac{1}{r^2} \frac{d}{dr}\left(r^2 \frac{d\Phi}{dr}\right) = \frac{d^2\Phi}{dr^2} + \frac{2}{r}\left(\frac{d\Phi}{dr}\right) = -\frac{e c_L}{\epsilon} \exp\left(-\frac{e\Phi}{k_B T}\right) \tag{19}$$

For comparison of particle spheres to particle cylinders, we have $a_1 = 3.12\ nm$, which gives for

the same β_1 a charge density that is 15% larger. When comparing solutions to the differential

equations, the term that is different between the spherical and cylindrical differential equations is

$\frac{2}{r}\frac{d\Phi}{dr}$ versus $\frac{1}{r}\frac{d\Phi}{dr}$. In either shape case, this term is dominated by the far-right side of Equation 19

for most of the potential distribution under reasonable surface-charge densities. The largest

discrepancy comes from treating the concentric volume of distance L away from the surface as a

cylinder or a sphere, but these are both similar in volume for aspect ratios close to unity. Thus, the

calculated L values due to changing particle shape are not importantly different.

With c_L determined from Equations 13-16 as outlined in SI, it remains to calculate the

molecular concentrations $c_m(y)$ in Equation 7, which are the local midpoint concentrations

between two flat plates of constant surface-charge density q in the Derjaguin approximation and

are determined from[24]

$$q = -\sqrt{2\epsilon k_B T c_m(y)} \tan\left(\frac{y}{2}\sqrt{\frac{e^2 c_m(y)}{2\epsilon k_B T}}\right) \tag{20}$$

Note that $c_m(y)$ is not a function of the size distribution, whereas L and c_L are. The y domain is

discretized, and the midpoint concentrations $c_m(y)$ are numerically evaluated as a function of y

from Equation 20. The integral in Equation 7 is subsequently evaluated for the particular distribution average cylindrical radius, R_C, in Equation 13. To obtain the prefactor of the integral in Equation 7 for each i, j particle pair, we replace the distribution ith and jth cylinder volumes with volume average radii a_i and a_j, respectively. This exercise gives the electrostatic interaction potential for each i, j particle pair in the distribution. The corresponding total interaction potential, $U_{tot}(r)$, for each pair follows from Equations 4-6.

3.4 Calculation of Nafion™ Transient Size Distributions

With each i, j total pair potential energy established, the rate constants and stability factors in Smoluchowski kinetics are known from Equations 2 and 3. Starting with a mixture of single chains and the values of ϕ and β_1, the Smoluchowski rate expression in Equation 1 is forward integrated in small time increments. At each new time step, new i, j total potential energies are calculated after determining new values for L, c_L, and $c_m(y)$ from Equations 10-16 and 20 in sequence. As particles grow larger and the distribution broadens in size, more and more i, j pairs appear, and the calculation becomes ever more involved. The SI summarizes the calculation procedure.

4. Results and Discussion

4.1 Size Distributions

Figure 6 plots the predicted time course of a typical Nafion™ average-volume spherical size distribution. In these calculations, Nafion™ concentration is 2 wt% ($\phi = 0.0081$) dissolved in a 50 wt% water/50 wt% n-propanol solvent. Relative permittivity values of all water/n-propanol mixtures are volume averaged between that of water (78.4) and that of n-propanol (20.2). Here β_1 is 0.63 meaning that 63% of the single chain sulfonate groups are externally exposed. This gives

an exposed surface charge density of $q = -0.214 \; C/m^2$. As noted above, larger aggregates trap more hydrogen ions as β_i varies inversely with $\sqrt[3]{i}$. Starting Nafion™ single-chain spherical radius is 3 nm.

Particle sizes in Figure 6 grow in time and the distribution broadens as the particles aggregate. After about 30 s, sizes only slowly increase. Effectively, the final size distribution stabilizes near 30 s, although minor changes are observed out to 100 s. The reason why this occurs is shown by the stability ratio, W, represented by the straight dashed line plotted on a logarithmic ordinate scale. Average-particle stability ratios grow exponentially large with increasing particle size kinetically choking further particle growth. Large stability ratios from Equation 3, in turn, arise from the large repulsive electrostatic potential energies when only a single counterion is present in solution.[24] The final distribution occurs quickly and is, therefore, characteristic of
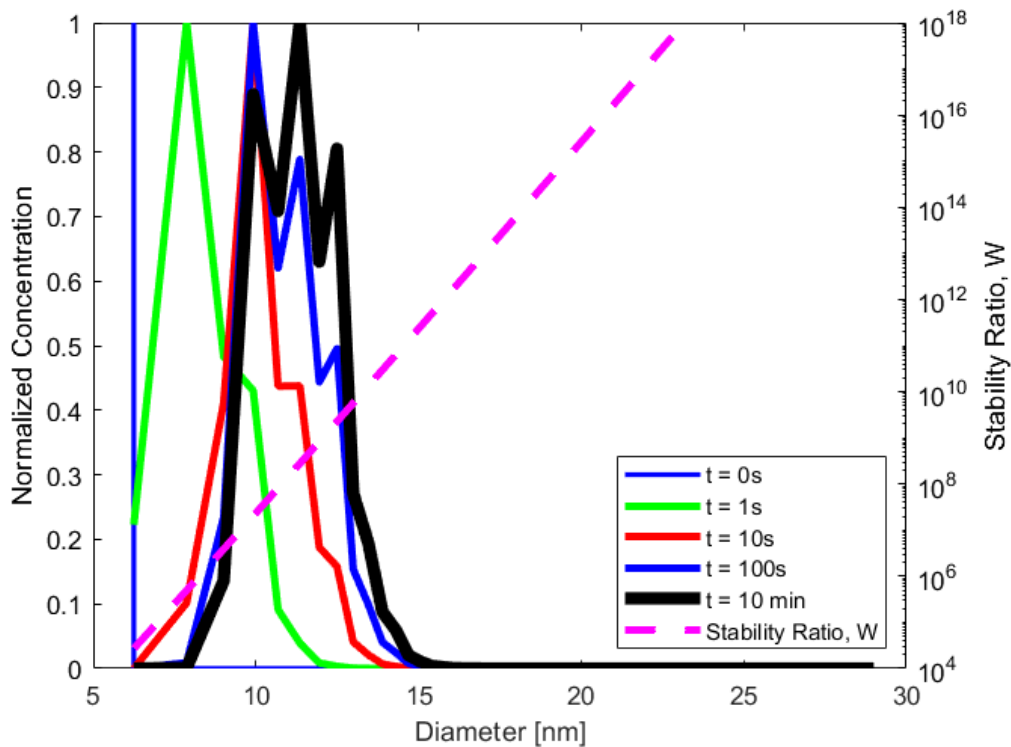
Figure 6: Model-predicted time evolution of size distributions and stability ratio for 2 wt% ($\phi = 0.0081$) Nafion™ suspended in a 50/50 wt% water/n-propanol solvent. Stability ratios are between particles of the same size at the final distribution.

Nafion™ solutions experienced in practice. No coagulation occurs because the final aggregated sizes are not large enough to settle under gravity, in agreement with our experimental observations.

Figure 7 shows final size distributions for two different dispersion concentrations of Nafion: 0.1 wt% ($\phi \sim 4 \times 10^{-4}$) in Figure 7A and 4 wt% ($\phi \sim 0.016$) in Figure 7B for two different solvent mixtures. Higher water-content solvents correspond to higher dielectric permittivities, smaller electrostatic energy barriers,[24] and, accordingly, larger particle sizes. The effect is surprisingly large. Further, particle sizes in the dilute suspension of 0.1 wt% (Figure 7A) are considerable smaller than those in the more concentrated suspension of 4 wt% (Figure 7B).[24]

This effect is also due to the single-ion potential energy barriers that, in accord with Figure 4, are much larger in dilute suspensions.[24] Comparison between the 30 and 90 wt% water solvents for 0.1 wt% Nafion™ affirms the idea that Nafion™ chains are mostly unaggregated or in small aggregates, yielding nearly uniform USAXS data for dilute systems, regardless of solvent water composition.[2]
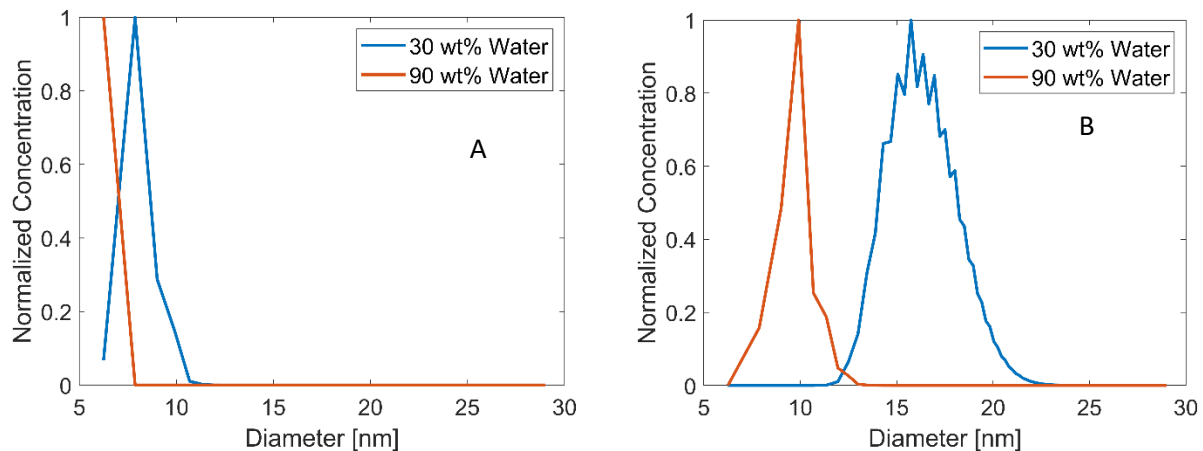
Figure 7: Model-predicted final particle-size distributions for (A) 0.1 wt% ($\phi \sim 4x10^{-4}$) and (B) 4 wt% ($\phi \sim 0.016$) Nafion™ in 30 wt% (blue) and 90 wt% (red) water.

Figure 8 illustrates how sensitive the final aggregate size is to the choice of the parameter β_1. Here, the average spherical diameter for the final distribution is plotted against β_1 values ranging from 0.01 to 1. As can be seen, the choice of β_1 does not significantly impact size distributions in the range above about 0.3. Indeed, taking $\beta_1 = 0.3$ or $\beta_1 = 1$ modifies the resultant aggregate size by less than 1 nm. As expected, for very low values of β_1, size distributions increase dramatically.
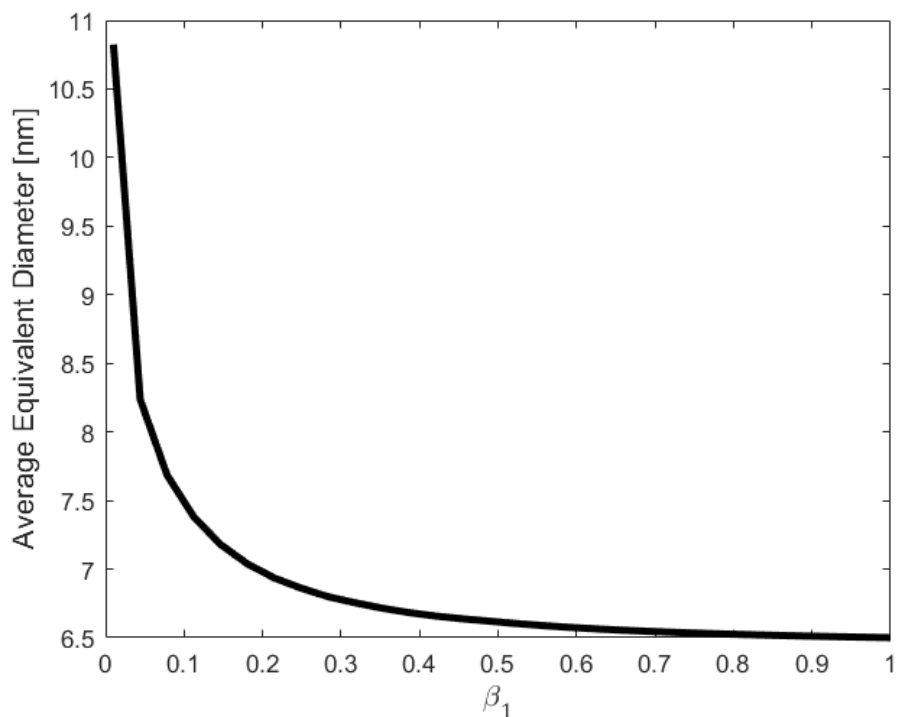

Figure 8: Model-predicted average final particle-size distributions as a function of β_1 for 50 wt% *n*-propanol in water at 1 wt% ($\phi = 0.00405$) Nafion™.

An experimental PFSA-ionomer size distribution is measured by Wawra *et al.* using analytic ultracentrifugation.[45] Although the size measurements by Wawra *et al.* are for Aquivion™

ionomers, their reported size distributions are in well accord with our predictions in Figures 6 through 8. In particular, aggregated Aquivion™ particle sizes remain small, less than 10 nm.[45] Overall, PFSA-ionomer experimental and predicted sizes confirm the presence of aggregated small particles in alcohol/water solvents that do not grow large enough to settle under gravity.

4.2 Suspension pH

It is commonly asserted that a pH probe measures the activities of protons in a liquid solution.[46] The relationship between proton activity and concentration has not been well explored when the probe interacts with double layers emanating from suspended particles in a solution. Here, we follow others[23] and assume that the measured proton activity corresponds to the average bulk-solution molar concentration in the Nafion™ suspension.[23] Accordingly, once the final, kinetically stable particle-size distribution is known, calculation of the suspension pH is straightforward. Only hydrogen ions released from the external surface of each aggregate contribute to solution pH. That is, only those hydrogen ions distributed in the diffuse layer neutralizing the external aggregate surface charge are detected by the pH probe. All remaining hydrogen ions trap inside the aggregates much as they do in Nafion™ membranes. As a result, the measured suspension pH in Figure 2 serves as a proxy for the final size distribution of Nafion™ colloidal aggregates.[23]

Let $\langle c_H \rangle$ represent the average molar concentration of hydrogen ions in the diffuse double layers of the suspension. Then suspension neutrality demands that

$$\langle c_H \rangle = -2\pi \frac{q}{e(1-\phi)} \sum_{i=1}^{N} C_i \, R_i (R_i + L_i) \tag{21}$$

Measured suspension pH then follows, after converting to molar units, as

$$\text{pH} \equiv -\log_{10}\langle c_H \rangle \tag{22}$$

Thus, dispersion pH emerges directly from the calculated final size distribution and Equations 21 and 22. Only one unknown parameter appears in the model predictions of the size distributions and pH: the single chain fraction of exposed sulfonate side groups: β_1. To ascertain β_1, we fit one measured pH datum from Figure 2 at 4 wt% Nafion™ and 90 wt% water, where the pH measurements are most accurate as they contain the largest concentration of hydronium ions and also the largest weight percent of water. This fit point is demarked as a red box in Figure 9 and yields a value of $\beta_1 = 0.63$ (*i.e.*, an exterior surface charge density of $q = -0.214\ C/m^2$). Equivalently, ~ 40% of the $-SO_3^-$-acid sites bury in the single chain consistent with a rod-like structure. Dashed lines in Figure 9 display the model calculations using only the single adjusted parameter. Agreement is excellent, not only correctly predicting the role of suspension concentration on dispersion pH but also the role of solvent composition. The dielectric permittivity is the largest contributor to the differences between the pH curves: higher dielectric constants lead to greater electrostatic repulsion, smaller particles sizes, and relatively less proton trapping. Some disagreement with theory is seen for the 90 wt% water solvent at higher pH values consistent with the larger reported experimental errors. Nevertheless, predicted pH values vary significantly with β_1 so our ability to match experimental pH is a sensitive test of the proposed model.
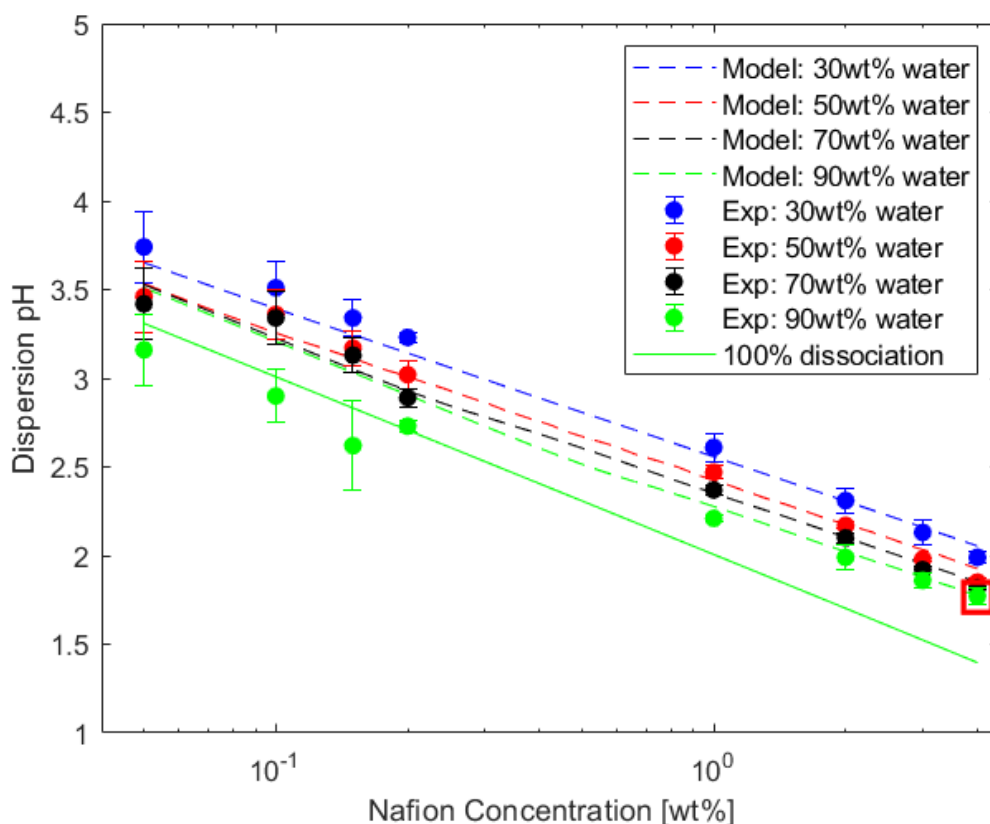
Figure 9: Dispersion experimental pH (filled circles) as a function of Nafion™ concentration in four water/*n*-propanol solutions after Berlinger *et al.*[23] (with permission) compared to model-predicted pH (dashed lines) The solid line for 90 wt % water corresponds to 100% dissociation of sulfonate side groups. A red box encompasses the datum used to determine β_1.

5. Conclusions

To rationalize the measured pH of Nafion™ polymer dissolved in mixed alcohol/water solvents, and, hence, the released solution protons from the Nafion™ colloidal particles, we propose a colloidal aggregation theory. In the proposed perikinetic Smoluchowski framework, Nafion™ polymer forms particles that grow until the repulsive electrostatic barriers between them prevent further growth. Accordingly, Nafion solutions, the precursors of current fuel-cell separation membranes and catalyst layers, are suspensions of kinetically stabilized aggregates. New particle

electrostatic potential energies are utilized from Part I, where only hydrogen ions released from the acidic polymer side chains are present in the solvent. Resulting single-counterion diffuse layers give rise to potential energies that are much larger than those in classical double layer theory and decrease with increasing suspension volume fraction. Predicted final particle sizes are in qualitative agreement with available measured distributions for Aquivion™ PFSA in aqueous electrolyte and are too small to settle under gravity as observed.

The key idea for understanding Nafion™-solution pH is particle aggregation that buries counterions internally: only external aggregate diffuse-layer hydrogen ions are detected by pH probes. Excellent agreement between measured pH and theory is achieved with a single adjusted parameter: a single chain exposed-ion percentage of $\beta_1 = 63\%$. Because particle sizes are insensitive to larger β_1 values, we have some confidence in the final sizes predicted. Thus, in agreement with literature, Nafion™ single chains display a folded structure with substantial hydrogen-ion burying that increases with aggregate size. In addition to aggregate trapping of hydrogen counterions, we observe that a main driver behind changes in pH is the dielectric permittivity, which drastically changes as the repulsive energies for different solvents and inversely correlates with aggregate size. Finally, this study further motivates the need to develop experimental techniques capable of interrogating the size and shape of colloidal Nafion™ particles, as they are critical precursors for controlling the structure of Nafion™ porous electrodes.

Supporting Information. Numerical details of the aggregation algorithm.

Acknowledgements

Nomenclature

a	Radius of sphere $[m]$
A_H	Hamaker Constant $[J]$
β	Fraction of protons dissociated
c_L	Number concentration of counterions per solvent volume at L $[1/m^3]$
c_m	Midpoint number concentration of counterions per solvent volume between two flat plates $[1/m^3]$
$\langle c_H \rangle$	Average molar concentration of hydrogen ions per unit solvent volume $[1/m^3]$
C_i	Number concentration of size i aggregate per suspension volume $[1/m^3]$
DLVO	Derjaguin-Landau-Verwey-Overbeek
e	Charge of an electron $[1.602 \times 10^{-19}\ C]$
ϵ_o	Free-space dielectric permittivity $[8.854 \cdot 10^{-12}\ C/V \cdot m]$
ϵ	Fluid dielectric permittivity $[C/V \cdot m]$
h	Separation distance between two flat plates $[m]$
$\hbar$	Reduced Planck's constant $(1.056 \times 10^{-34} J \cdot s)$
k_B	Boltzmann constant $(1.38 \times 10^{-23}\ J/K)$
K_{ij}	Diffusion-based aggregation kinetic rate constant between particles i and j $[m^3/s]$
L	Dissociation distance of counterions away from a flat plate $[m]$
L_i	Length of cylinder of i chain $[m]$
λ	Debye length $[m]$
n	index of refraction
N_A	Avogadro's number $(6.022 \times 10^{23}\ mol^{-1})$
$N_{SO_3^-}$	Number of equivalents per single chain
μ	Viscosity $[Pa \cdot s]$
ν_e	Absorption frequency $(5 \times 10^{15}\ s^{-1})$
pH	Log normalized average proton concentration $-log_{10}(\langle c_H \rangle)$

pH_L Log normalized proton concentration at $L - log_{10}(c_{H^+,L})$

ϕ Volume fraction of particles

Φ Potential $[V]$

q Surface-charge density $[C/m^2]$

r Radial distance from center of cylinder $[m]$

ρ Density $[kg/m^3]$

R Ideal gas constant (8.314 $J/mol \cdot K$)

R_i Radius of cylinder of i chains $[m]$

R_C Average radius of ionomer chains $[m]$

T Temperature $[K]$

U_r Repulsive energy between two spheres $[J]$

U_{tot} Total interaction energy between two spheres $[J]$

U_{vdw} Attractive van-der-Waals energy between two spheres $[J]$

w_i Weight Fraction of species i

W_{ij} Stability ratio between particles i and j

y Linear distance between two flat plates $[m]$

References

(1)   Van Cleve, T.; Khandavalli, S.; Chowdhury, A.; Medina, S.; Pylypenko, S.; Wang, M.; More, K. L.; Kariuki, N.; Myers, D. J.; Weber, A. Z.; Mauger, S. A.; Ulsh, M.; Neyerlin, K. C. Dictating Pt-Based Electrocatalyst Performance in Polymer Electrolyte Fuel Cells, from Formulation to Application. *ACS Appl. Mater. Interfaces* **2019**, *11* (50), 46953–46964. https://doi.org/10.1021/acsami.9b17614.

(2)   Berlinger, S. A.; Dudenas, P. J.; Bird, A.; Chen, X.; Freychet, G.; McCloskey, B. D.; Kusoglu, A.; Weber, A. Z. Impact of Dispersion Solvent on Ionomer Thin Films and Membranes. *ACS Appl. Polym. Mater.* **2020**, *2* (12), 5824–5834. https://doi.org/10.1021/acsapm.0c01076.

(3)   Holdcroft, S. Fuel Cell Catalyst Layers: A Polymer Science Perspective. *Chem. Mater.* **2014**, *26* (1), 381–393. https://doi.org/10.1021/cm401445h.

(4)   Ngo, T. T.; Yu, T. L.; Lin, H.-L. Influence of the Composition of Isopropyl Alcohol/Water Mixture Solvents in Catalyst Ink Solutions on Proton Exchange Membrane Fuel Cell Performance. *Journal of Power Sources* **2013**, *225*, 293–303. https://doi.org/10.1016/j.jpowsour.2012.10.055.

(5)   Shin, S.-J.; Lee, J.-K.; Ha, H.-Y.; Hong, S.-A.; Chun, H.-S.; Oh, I.-H. Effect of the Catalytic Ink Preparation Method on the Performance of Polymer Electrolyte Membrane Fuel Cells. *Journal of Power Sources* **2002**, *106* (1), 146–152. https://doi.org/10.1016/S0378-7753(01)01045-X.

(6)   Uchida, M.; Aoyama, Y.; Eda, N.; Ohta, A. New Preparation Method for Polymer-Electrolyte Fuel Cells. *J. Electrochem. Soc.* **1995**, *142* (2), 463. https://doi.org/10.1149/1.2044068.

(7)   Gao, X.; Yamamoto, K.; Hirai, T.; Ohta, N.; Uchiyama, T.; Watanabe, T.; Imai, H.; Sugawara, S.; Shinohara, K.; Uchimoto, Y. Impact of the Composition of Alcohol/Water Dispersion on the Proton Transport and Morphology of Cast Perfluorinated Sulfonic Acid Ionomer Thin Films. *ACS Omega* **2021**, *6* (22), 14130–14137. https://doi.org/10.1021/acsomega.1c00607.

(8)   Kim, Y. S.; Welch, C. F.; Hjelm, R. P.; Mack, N. H.; Labouriau, A.; Orler, E. B. Origin of Toughness in Dispersion-Cast Nafion Membranes. *Macromolecules* **2015**, *48* (7), 2161–2172. https://doi.org/10.1021/ma502538k.

(9)   Silva, R. F.; De Francesco, M.; Pozio, A. Solution-Cast Nafion® Ionomer Membranes: Preparation and Characterization. *Electrochimica Acta* **2004**, *49* (19), 3211–3219. https://doi.org/10.1016/j.electacta.2004.02.035.

(10)   Moore, R. B.; Martin, C. R. Chemical and Morphological Properties of Solution-Cast Perfluorosulfonate Ionomers. *Macromolecules* **1988**, *21* (5), 1334–1339. https://doi.org/10.1021/ma00183a025.

(11)   Merlo, L.; Ghielmi, A.; Arcella, V. FUEL CELLS – PROTON-EXCHANGE MEMBRANE FUEL CELLS | Membranes: Advanced Fluorinated. In *Encyclopedia of Electrochemical Power Sources*; Garche, J., Ed.; Elsevier: Amsterdam, 2009; pp 680–699. https://doi.org/10.1016/B978-044452745-5.00930-8.

(12)   Wang, S.; Sun, G.; Wu, Z.; Xin, Q. Effect of Nafion® Ionomer Aggregation on the Structure of the Cathode Catalyst Layer of a DMFC. *Journal of Power Sources* **2007**, *165* (1), 128–133. https://doi.org/10.1016/j.jpowsour.2006.11.067.

(13)   Xie, Z.; Navessin, T.; Zhao, X.; Adachi, M.; Holdcroft, S.; Mashio, T.; Ohma, A.; Shinohara, K. Nafion Ionomer Aggregation and Its Influence on Proton Conduction and Mass Transport in Fuel Cell Catalyst Layers. *ECS Trans.* **2008**, *16* (2), 1811. https://doi.org/10.1149/1.2982022.

(14)   Yamaguchi, M.; Terao, T.; Ohira, A.; Hasegawa, N.; Shinohara, K. Size and Shape of Nafion Particles in Water after High-Temperature Treatment. *J Polymer Science Part B: Polymer Physics* **2019**, *57* (13), 813–818. https://doi.org/10.1002/polb.24833.

(15)   Yamaguchi, M.; Matsunaga, T.; Amemiya, K.; Ohira, A.; Hasegawa, N.; Shinohara, K.; Ando, M.; Yoshida, T. Dispersion of Rod-like Particles of Nafion in Salt-Free Water/1-Propanol and Water/Ethanol Solutions. *J. Phys. Chem. B* **2014**, *118* (51), 14922–14928. https://doi.org/10.1021/jp506814m.

(16) Welch, C.; Labouriau, A.; Hjelm, R.; Orler, B.; Johnston, C.; Kim, Y. S. Nafion in Dilute Solvent Systems: Dispersion or Solution? *ACS Macro Lett.* **2012**, *1* (12), 1403–1407. https://doi.org/10.1021/mz3005204.

(17) Gupit, C. I.; Li, X.; Maekawa, R.; Hasegawa, N.; Iwase, H.; Takata, S.; Shibayama, M. Nanostructures and Viscosities of Nafion Dispersions in Water/Ethanol from Dilute to Concentrated Regimes. *Macromolecules* **2020**, *53* (4), 1464–1473. https://doi.org/10.1021/acs.macromol.9b02314.

(18) Kusoglu, A.; Weber, A. Z. New Insights into Perfluorinated Sulfonic-Acid Ionomers. *Chem. Rev.* **2017**, *117* (3), 987–1104. https://doi.org/10.1021/acs.chemrev.6b00159.

(19) Aldebert, P.; Dreyfus, B.; Pineri, M. Small-Angle Neutron Scattering of Perfluorosulfonated Ionomers in Solution. *Macromolecules* **1986**, *19* (10), 2651–2653. https://doi.org/10.1021/ma00164a035.

(20) Aldebert, P.; Dreyfus, B.; Gebel, G.; Nakamura, N.; Pineri, M.; Volino, F. Rod like Micellar Structures in Perfluorinated Ionomer Solutions. *J. Phys. France* **1988**, *49* (12), 2101–2109. https://doi.org/10.1051/jphys:0198800490120210100.

(21) Gebel, G.; Loppinet, B. Colloidal Structure of Ionomer Solutions in Polar Solvents. *Journal of Molecular Structure* **1996**, *383* (1–3), 43–49. https://doi.org/10.1016/S0022-2860(96)09266-6.

(22) Loppinet, B.; Gebel, G. Rodlike Colloidal Structure of Short Pendant Chain Perfluorinated Ionomer Solutions. *Langmuir* **1998**, *14* (8), 1977–1983. https://doi.org/10.1021/la9710987.

(23) Berlinger, S. A.; McCloskey, B. D.; Weber, A. Z. Inherent Acidity of Perfluorosulfonic Acid Ionomer Dispersions and Implications for Ink Aggregation. *J. Phys. Chem. B* **2018**, *122* (31), 7790–7796. https://doi.org/10.1021/acs.jpcb.8b06493.

(24) Srivastav, H.; Weber, A. Z.; Radke, C. J. Colloidal Stability of PFSA-Ionomer Dispersions Part I: Single-Ion Electrostatic Interaction Potential Energies, Submitted. *Langmuir* **2023**.

(25) Dorenbos, G.; Suga, Y. Simulation of Equivalent Weight Dependence of Nafion Morphologies and Predicted Trends Regarding Water Diffusion. *Journal of Membrane Science* **2009**, *330* (1), 5–20. https://doi.org/10.1016/j.memsci.2008.11.056.

(26) David E. Moilanen; Ivan R. Piletic, and; Fayer*, M. D. *Water Dynamics in Nafion Fuel Cell Membranes: The Effects of Confinement and Structural Changes on the Hydrogen Bond Network†*. ACS Publications. https://doi.org/10.1021/jp067460k.

(27) Safronova, E. Y.; Voropaeva, D. Y.; Safronov, D. V.; Stretton, N.; Parshina, A. V.; Yaroslavtsev, A. B. Correlation between Nafion Morphology in Various Dispersion Liquids and Properties of the Cast Membranes. *Membranes* **2023**, *13* (1), 13. https://doi.org/10.3390/membranes13010013.

(28) Lin, H.-L.; Yu, T. L.; Huang, C.-H.; Lin, T.-L. Morphology Study of Nafion Membranes Prepared by Solutions Casting. *Journal of Polymer Science Part B: Polymer Physics* **2005**, *43* (21), 3044–3057. https://doi.org/10.1002/polb.20599.

(29) Gebel, G. Structural Evolution of Water Swollen Perfluorosulfonated Ionomers from Dry Membrane to Solution. *Polymer* **2000**, *41* (15), 5829–5838. https://doi.org/10.1016/S0032-3861(99)00770-3.

(30) Matos, B. R.; Santiago, E. I.; Rey, J. F. Q.; Fonseca, F. C. Origin of α and β Relaxations of Nafion. *Phys. Rev. E* **2014**, *89* (5), 052601. https://doi.org/10.1103/PhysRevE.89.052601.

(31) Li, S.; Terao, K.; Sato, T. Colloidal Dispersion of a Perfluorosulfonated Ionomer in Water–Methanol Mixtures. *Polymers (Basel)* **2018**, *10* (1), 72. https://doi.org/10.3390/polym10010072.

(32) Melo, L. G. A.; Hitchcock, A. P. Electron Beam Damage of Perfluorosulfonic Acid Studied by Soft X-Ray Spectromicroscopy. *Micron* **2019**, *121*, 8–20. https://doi.org/10.1016/j.micron.2019.02.006.

(33) Yakovlev, S.; Balsara, N. P.; Downing, K. H. Insights on the Study of Nafion Nanoscale Morphology by Transmission Electron Microscopy. *Membranes* **2013**, *3* (4), 424–439. https://doi.org/10.3390/membranes3040424.

(34) Klein, J. M.; Welch, C.; Ponnurangam, S.; Tarokh, A.; Karan, K.; Hawley, M. E.; Sokolova, A.; Yim, S.-D.; Hjelm, R. P.; Kim, Y. S. Colloidal Nafion Particles: Are Cylinders Ubiquitous? *ACS Macro Lett.* **2023**, *12* (12), 1648–1653. https://doi.org/10.1021/acsmacrolett.3c00616.

(35) Yang, D.; Guo, Y.; Tang, H.; Yang, D.; Ming, P.; Zhang, C.; Li, B.; Zhu, S. Effect of Rheological Properties of Catalyst Slurry on the Structure of Catalyst Layer in PEMFC. *International Journal of Hydrogen Energy* **2022**, *47* (14), 8956–8964. https://doi.org/10.1016/j.ijhydene.2021.12.227.

(36) Kruyt, Hugor. Electrochemistry of the Double Layer. In *Colloid Science. Volume 1: Irreversible Systems*; Elsevier Publishing Company, 1952; Vol. 1, pp 115–146.

(37) Berg, J. C. Kinetics of Aggregation. In *An Introduction to Interfaces and Colloids: The Bridge to Nanoscience*; World Scientific, 2009; pp 560–582. https://doi.org/10.1142/7579.

(38) Shukla, S.; Bhattacharjee, S.; Weber, A. Z.; Secanell, M. Experimental and Theoretical Analysis of Ink Dispersion Stability for Polymer Electrolyte Fuel Cell Applications. *J. Electrochem. Soc.* **2017**, *164* (6), F600–F609. https://doi.org/10.1149/2.0961706jes.

(39) Marmur, A. A Kinetic Theory Approach to Primary and Secondary Minimum Coagulations and Their Combination. *Journal of Colloid and Interface Science* **1979**, *72* (1), 41–48. https://doi.org/10.1016/0021-9797(79)90178-4.

(40) Israelachvili, J. N. Electrostatic Forces between Surfaces in Liquids. In *Intermolecular and Surface Forces*; Elsevier, 2011; pp 291–340. https://doi.org/10.1016/B978-0-12-375182-9.10014-4.

(41) Maryott, A. A.; Smith, E. R. *Circular of the Bureau of Standards No. 514: Table of Dielectric Constants of Pure Liquids*; National Bureau of Standards, 1951.

(42) PubChem. *1-Propanol*. https://pubchem.ncbi.nlm.nih.gov/compound/1031 (accessed 2023-08-30).

(43) *Refractive Indices of Water and Aqueous Electrolyte Solutions under High Magnetic Fields*. https://doi.org/10.1021/jp0310145.

(44) Nafion-D520-D521-D1020-D1021-D2020-D2021-p-14-Product-Info.Pdf. https://www.nafion.com/en/-/media/files/nafion/nafion-d520-d521-d1020-d1021-d2020-d2021-p-14-product-info.pdf?rev=281266378f984bb681c16b4c73d61565&hash=B5506B26E9B1E2C5634546C3C73DF6C9 (accessed 2024-02-12).

(45) Wawra, S. E.; Thoma, M.; Walter, J.; Lübbert, C.; Thajudeen, T.; Damm, C.; Peukert, W. Ionomer and Protein Size Analysis by Analytical Ultracentrifugation and Electrospray Scanning Mobility Particle Sizer. *Eur Biophys J* **2018**, *47* (7), 777–787. https://doi.org/10.1007/s00249-018-1314-2.

(46) *pH Electrode Theory from Cole-Parmer*. https://www.coleparmer.com/tech-article/ph-electrode-theory (accessed 2023-08-21).

TOC Graphic